

See discussions, stats, and author profiles for this publication at: <https://www.researchgate.net/publication/285581796>

# Generalized photon sieves: Fine control of complex fields with simple pinhole arrays

Article in *Optica* · December 2015

DOI: 10.1364/OPTICA.2.001028

CITATIONS

5

READS

215

4 authors, including:



**Ruifeng Liu**

Xi'an Jiaotong University

32 PUBLICATIONS 133 CITATIONS

[SEE PROFILE](#)



**Miles John Padgett**

University of Glasgow

628 PUBLICATIONS 20,077 CITATIONS

[SEE PROFILE](#)



**David Benjamin Phillips**

University of Exeter

59 PUBLICATIONS 533 CITATIONS

[SEE PROFILE](#)

Some of the authors of this publication are also working on these related projects:



Single-pixel Imaging [View project](#)



Orbital angular momentum of light [View project](#)

All content following this page was uploaded by [Miles John Padgett](#) on 03 December 2015.

The user has requested enhancement of the downloaded file.

# Generalized photon sieves: fine control of complex fields with simple pinhole arrays

R. LIU,<sup>1,2</sup> F. LI,<sup>2</sup> M. J. PADGETT,<sup>1</sup> AND D. B. PHILLIPS<sup>1,\*</sup>

<sup>1</sup>SUPA, School of Physics and Astronomy, University of Glasgow, Glasgow G12 8QQ, UK

<sup>2</sup>Department of Applied Physics, School of Science, Xi'an Jiaotong University, Xi'an, Shaanxi, China

\*Corresponding author: david.phillips@glasgow.ac.uk

Received 10 August 2015; revised 6 October 2015; accepted 19 October 2015 (Doc. ID 247558); published 3 December 2015

Spatial shaping of light beams has led to numerous new applications in fields such as imaging, optical communication, and micromanipulation. However, structured radiation is less well explored beyond visible optics, where methods for shaping fields are more limited. Binary amplitude filters are often used in these regimes and one such example is a photon sieve consisting of an arrangement of pinholes, the positioning of which can tightly focus incident radiation. Here, we describe a method to design generalized photon sieves: arrays of pinholes that generate arbitrary structured complex fields at their foci. We experimentally demonstrate this approach by the production of Airy and Bessel beams, and Laguerre–Gaussian and Hermite–Gaussian modes. We quantify the beam fidelity and photon sieve efficiency, and also demonstrate control over additional unwanted diffraction orders and the incorporation of aberration correction. The fact that these photon sieves are robust and simple to construct will be useful for the shaping of short- or long-wavelength radiation and eases the fabrication challenges set by more intricately patterned binary amplitude masks. © 2015 Optical Society of America

**OCIS codes:** (050.1965) Diffractive lenses; (050.4865) Optical vortices; (230.1950) Diffraction gratings.

<http://dx.doi.org/10.1364/OPTICA.2.001028>

## 1. INTRODUCTION

Control over spatial structuring of the amplitude and phase of coherent light has revealed a host of novel phenomena and applications. For example, Bessel and Airy beams exhibit pseudonondiffracting propagation and self-healing if obstructed [1–5]. These two properties have been used to extend depth of field in bright-field and light-sheet microscopy and increase image quality deep into scattering tissue, along with a range of other applications [6–10]. Another family of beams includes those with helical wavefronts which carry orbital angular momentum (OAM). These beams have been used to achieve superresolution-stimulated emission depletion microscopy [11], increase the data capacity of communication channels [12], exert torque on microscopic particles [13], and measure rotation rate of spinning objects [14,15]. There is now increasing interest in exploring how novel-structured fields such as the types just described interact with matter outside the optical regime [16–20].

Spatial structuring of the amplitude and phase of light is routinely achieved by modulating the phase of an incident beam using a phase-only spatial light modulator (SLM) [21,22]. Prior to the application of phase-only SLMs, it was shown in the 1960s that binary amplitude masks can also be used to shape both the amplitude and phase of light. For example, the *computer-generated hologram method* encodes amplitude and phase in a binary grating by locally varying the duty cycle of the grating to control the diffracted amplitude and the lateral phase of the grating to control

the optical phase of the diffracted light [23–26]. Such binary patterns have recently been implemented on digital micromirror devices (DMDs) to take advantage of their high switching rates [27]. Since the development of phase-only SLMs and DMDs has been driven by growth in commercial display technologies, beam-shaping options become more limited outside of the near-visible spectrum. For example, to achieve spatial structuring of electron beams and X-rays, individually fabricated high-resolution binary amplitude masks are often required [28–30].

In this paper, we demonstrate how simple pinhole arrays can be used to generate arbitrarily structured complex scalar fields, focused to predefined distances behind the array. Our proposed concept is a generalization of a photon sieve that was first introduced by Kipp *et al.* in 2001 [16]. The original photon sieve was a binary amplitude lens consisting of an arrangement of pinholes, each positioned such that light emanating from it contributed positively to the on-axis field at the focus of the sieve. As discussed in [16], using pinholes allows the diameter of a photon sieve to be extended beyond the diameter of a Fresnel zone plate of equivalent resolution, and therefore the photon sieve achieves a tighter focus due to the increased numerical aperture (NA). Since their invention, photon sieves have received much attention as they are particularly suitable for tight focusing and imaging with X-ray radiation [31,32]. Photon sieves are also simple to manufacture since they have a self-supporting structure containing no disconnected material in their design. In our work, instead of achieving

enhanced focusing using many thousands of pinholes as demonstrated in [16], we describe the design of general photon sieves containing a few hundred pinholes that create arbitrarily structured beams at their foci. Our method arranges the pinholes in a way that ensures the diffraction order containing the target field forms the brightest region of the diffraction pattern, while light radiated into other orders is still localized well enough to be separated from the target field. We also show how the positions of pinholes can be modified to incorporate aberration correction to rectify known phase distortions in the optical system.

We first review the design of a generalized binary Fresnel zone plate to generate an arbitrary (and therefore not necessarily circularly symmetric) spatially structured complex field at its focus. We then describe how a generalized Fresnel zone plate can be coarse-grained into pinholes to create an easily manufactured and robust photon sieve.

## 2. GENERALIZED FRESNEL ZONE PLATES

Much work has previously been carried out on the design of novel Fresnel zone plates, for example, to achieve a sharp Gaussian focus [33], to create pseudo-nondiffracting beams [34], and to control dispersion [35]. For the creation of an arbitrary scalar target field  $\mathcal{A}(x, y) = A(x, y)e^{i\phi_A(x, y)}$  [where  $A(x, y)$  and  $\phi_A(x, y)$  are the required amplitude and phase, respectively], a *binary transmittance function*,  $T(x, y)$ , encoding  $\mathcal{A}(x, y)$  in its first diffraction order, can be calculated using the computer-generated hologram method [24]:

$$T(x, y) = \frac{1}{2} + \frac{1}{2} \operatorname{sgn}[\cos(p(x, y)) + \cos(q(x, y))], \quad (1)$$

$$p(x, y) = \phi_A(x, y) + \phi_{\text{tilt}}(x, y), \quad (2)$$

$$q(x, y) = \arcsin(A(x, y)/A_{\max}), \quad (3)$$

where  $\operatorname{sgn}(x)$  is the sign function and  $A_{\max}$  is the maximum of amplitude  $A(x, y)$ , which serves to normalize the amplitude to between 0 and 1. As  $T(x, y)$  typically only has a partial overlap with the target field, light is also radiated into additional diffraction orders. To prevent the target field interfering with these other orders, it can be steered off-axis by incorporating a linear phase ramp given by  $\phi_{\text{tilt}}(x, y) = 2\pi(u_0x + v_0y)$ . Here,  $u_0$  and  $v_0$  are constants determining the gradient of the phase ramp. In the far field of the mask  $T(x, y)$ , providing that the functions  $p(x, y)$  and  $q(x, y)$  vary at a slower rate than  $\sqrt{(u_0^2 + v_0^2)}$ , the Fourier transform of the target field will be separated from additional orders. Therefore, by spatially filtering the field transmitted by  $T(x, y)$  when it is illuminated with a plane wave, the target field can be recovered in an image plane of the mask.

A similar approach can be used to design a binary transmittance function that *focuses* an arbitrary complex field  $\mathcal{A}(x, y)$  to a prescribed distance  $f$  beyond it: a *generalized Fresnel zone plate*. To illustrate this, we describe the design of a Fresnel zone plate to create an Airy beam, as recently the generation of Airy beams outside visible wavelengths has attracted increasing attention [29]. To design a generalized Fresnel zone plate, we first consider the fields propagating through a simple optical system consisting of a single lens, which Fourier transforms a complex field at the back focal plane of the lens (referred to here as the near field) to the front focal plane of the lens (the far field), where the target field will be created. Our generalized Fresnel zone plate

of focal length  $f$  will be placed at the plane corresponding to that of the Fourier transforming lens, a distance  $f$  behind the target field. Therefore, we first consider the field at the back focal plane, which is given by the Fourier transform of the target field:  $\mathcal{B}(x, y) = \mathcal{F}(\mathcal{A}(x, y))$ . In the following, the coordinates of  $\mathcal{B}$  have been scaled to real-space units, assuming that the Fourier transform has been performed with a lens of focal length  $f$ . The Fourier transform of a finite-energy approximation to a 2D Airy beam,  $\mathcal{B}_{\text{Airy}}(x, y)$ , has a Gaussian amplitude modulated with a cubic phase term as shown in Fig. 1(a) [5]. Therefore

$$\mathcal{B}_{\text{Airy}}(x, y) = B_0 e^{-\sqrt{x^2 + y^2}/\omega_0} e^{i\zeta(x^3 + y^3)}, \quad (4)$$

where  $B_0$  is the peak amplitude,  $\omega_0$  is the beam waist of the Gaussian, and  $\zeta$  is a constant scaling factor mapping lateral position to phase. The ratio of  $\omega_0$  and  $\zeta$  controls the propagation characteristics of the Airy beam, such as its quasi-diffraction-free propagation length and degree of apparent sideways acceleration (see [5] for more detail). In particular, increasing the magnitude of  $\zeta$  while keeping  $\omega_0$  constant increases the nondiffracting propagation length of the Airy beam and correspondingly the number of lobes visible in its cross-section. Here, these parameters have been chosen to generate the Airy beam depicted in Figs. 1(f)–1(h). We now calculate the field at the intermediate plane of the Fourier-transforming lens,  $\mathcal{C}(x, y) = \mathcal{C}(x, y) \exp i\phi_C(x, y)$ , which also corresponds to the plane at which our generalized Fresnel zone plate will be located.  $\mathcal{C}_{\text{Airy}}(x, y)$  is shown in Fig. 1(b) and has been calculated by numerically propagating  $\mathcal{B}_{\text{Airy}}(x, y)$  a distance  $f$  using the discrete angular spectrum method [36]. The effect of the Fourier-transforming lens is equivalent to the addition of a quadratic phase term,

$$\phi_{\text{lens}}(x, y, f) = \frac{2\pi}{\lambda} [f - (f^2 + x^2 + y^2)^{1/2}], \quad (5)$$

where  $\lambda$  is the wavelength of the incident radiation. We now incorporate this focusing term into our design field, yielding  $\mathcal{C}_{\text{Airy}}(x, y) \exp(i\phi_{\text{lens}}(x, y))$ , which is shown in Fig. 1(c). We can now binarize this field using Eq. (1) with inputs

$$p(x, y) = \phi_C(x, y) + \phi_{\text{tilt}}(x, y) + \phi_{\text{lens}}(x, y), \quad (6)$$

$$q(x, y) = \arcsin[\mathcal{C}(x, y)/C_{\max}], \quad (7)$$

which yields  $T_{\text{ZP}}(x, y)$ , the binary transmittance function of a Fresnel zone plate which encodes our target field,  $\mathcal{A}(x, y)$ , generated at its focus. If the NA of the focusing is low, then our target field is not tightly focused and interference with other unwanted on-axis diffraction orders will not be negligible. Therefore, as just described, adding a phase tilt to the field,  $\phi_{\text{tilt}}(x, y)$ , can be used to separate the diffraction orders within the focal plane, which moves the position of the diffraction order containing the focused target field off-axis.

Figure 1 shows how the procedure just described can be used to design a Fresnel zone plate that will create an Airy beam at its focus: an *Airy Fresnel zone plate*. Figure 1(i) shows the field calculated at the plane of the Fresnel zone plate,  $\mathcal{C}_{\text{Airy}}(x, y) \exp i(\phi_{\text{lens}} + \phi_{\text{tilt}})$ . This is then binarized using Eq. (1), yielding  $T_{\text{AiryZP}}(x, y)$ , the binary transmittance function of an off-axis Airy Fresnel zone plate, shown in Fig. 1(j). Figure 1(k) shows a simulation of the intensity of the Fresnel diffraction pattern at the focal plane of the Airy Fresnel zone plate when it is illuminated with a plane wave. The target Airy beam is created in the +1st

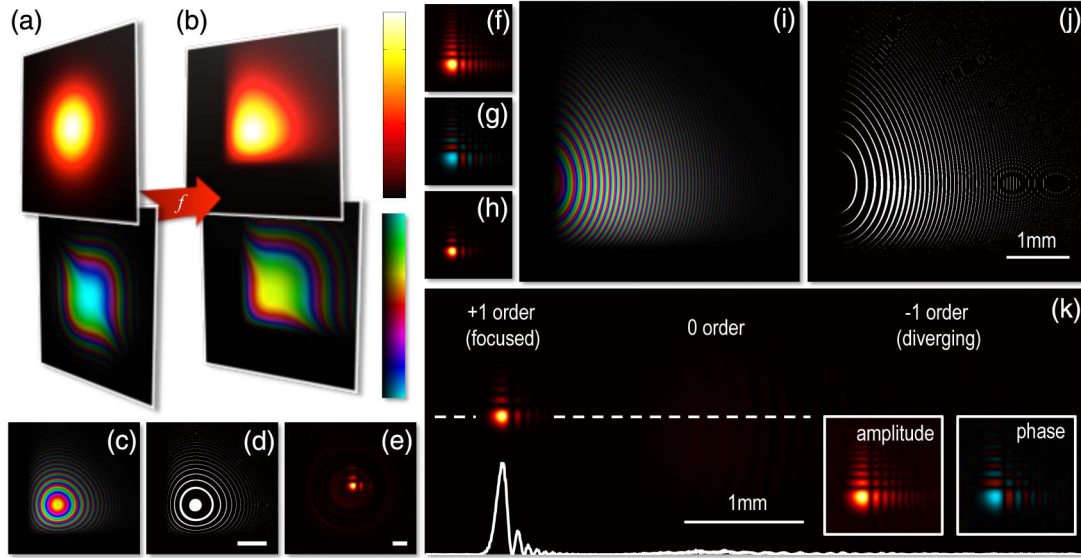


**Fig. 1.** Design of a Fresnel zone plate to generate an Airy beam at its focus. (a) Gaussian amplitude (upper panel) and cubic phase (lower panel) of  $\mathcal{B}_{\text{Airy}}(x, y)$ . Upper scale bar denotes relative amplitude. Lower scale bar denotes phase as color over a  $2\pi$  range and relative amplitude as brightness. These scale bars are also used throughout the other figures in this paper. (b) Amplitude and phase of  $\mathcal{C}_{\text{Airy}}(x, y)$ , resulting from the propagation of  $\mathcal{B}_{\text{Airy}}(x, y)$  a distance  $f$  in free space. (c) Phase of the field  $\mathcal{C}_{\text{Airy}} \exp i\phi_{\text{lens}}$ . (d) Binary transmittance function of an *on-axis* Airy Fresnel zone plate calculated directly from (c) without the incorporation of a phase tilt. (e) Simulation of the intensity at the focal plane of (d). Relative intensity is indicated using the same color map as (a). In this case, the on-axis Airy beam interferes with other on-axis diffraction orders, reducing its fidelity. Scale bars in (d) and (e) represent 1 mm. (f)–(h) Amplitude, phase, and intensity of the target field: an Airy beam generated with parameters  $\omega_0 = 0.01$  m,  $\zeta = 3.5 \times 10^9$  rad/m<sup>3</sup>,  $f = 0.25$  m. (i) Phase of the field  $\mathcal{C}_{\text{Airy}} \exp i(\phi_{\text{lens}} + \phi_{\text{tilt}})$ . (j)  $T_{\text{AiryZP}}$ , an *off-axis* Airy Fresnel zone plate, calculated from (i) using Eqs. (1)–(3). (k) Simulated intensity at the focal plane of (j). The Airy beam is now well separated from other diffraction orders, therefore maintaining a high fidelity. The border plot highlights the relative intensity along the dashed horizontal line through the center of the diffraction pattern. The simulated amplitude and phase of the generated beam (at a plane tilted normal to its propagation direction) is shown as insets for comparison with the target field in (f) and (g).

order (the amplitude and phase of the first order are shown in the insets). The 0th order of this mask is unfocused, and the -1st order is diverging.

### A. Beam Fidelity

The normalized fidelity  $F$  quantifies how faithfully the target field is generated ( $0 \leq F \leq 1$ , where 1 represents perfectly correlated complex fields). This can be calculated from the overlap integral of the target complex field  $U(x, y)$ , and the complex field actually generated by the generalized Fresnel zone plate  $V(x, y)$ , in the first order of the diffraction pattern:

$$F = \left| \frac{1}{N_F} \iint U(x, y) V^*(x, y) dx dy \right|^2, \quad (8)$$

$$N_F = \left[ \iint |U(x, y)|^2 dx dy \times \iint |V(x, y)|^2 dx dy \right]^{\frac{1}{2}}, \quad (9)$$

where  $N_F$  is the normalization constant and the limits of the integrals are determined by the region of interest around the first order of the diffraction pattern.

Using Eq. (8), the theoretical fidelity of the Airy beam generated by the Airy Fresnel zone plate  $T_{\text{AiryZP}}(x, y)$  is  $F = 0.99$ . This is slightly lower than 1 due to the small amount of light scattered into the region of the Airy beam from the other diffraction orders.  $F$  increases as the target field is tilted further off-axis and the diffraction orders are further separated. Conversely, if the target field is not tilted off-axis, the fidelity of the generated beam is severely reduced to  $F = 0.70$  by interference with other on-axis diffraction orders [as shown in Figs. 1(d) and 1(e)].

### 3. GENERALIZED PHOTON SIEVES

We now describe how the method illustrated in Section 2 can be further adapted to design generalized photon sieves that encode arbitrary complex fields at their foci. Evidently, the Airy Fresnel zone plate shown in Fig. 1(j) can be coarse-grained into pinholes positioned along the grating apertures. A similar approach has been used, for example, to coarse-grain an on-axis spiral Fresnel zone plate into a small number of pinholes to create beams carrying OAM [37]. While this produces an approximation to the required beam, the precise positioning of the pinholes will introduce additional diffraction orders into the radiated diffraction pattern, which may interfere with the target field and/or create unwanted additional intensity peaks at the focal plane. Here, we now describe a direct method (without the need for any iterative refinement) to calculate the position of pinholes in order to ensure that these additional diffraction orders are well controlled, preserving the formation of a high-fidelity target field.

The choice of pinhole positions relies on a basic principle: we consider the interference field created by two beams incident with tilts about orthogonal axes, as shown in Fig. 2(a). Here, we take the *primary* beam as the field focusing to produce the target field as just described, traveling with some tilt ( $\theta_1$ ) with respect to the optical axis [for example, Fig. 1(i) showing  $\mathcal{C}_{\text{Airy}}(x, y) \exp i(\phi_{\text{lens}} + \phi_{\text{tilt}})$ ]. We now consider a *secondary* beam, traveling with a tilt ( $\theta_2$ ) about an orthogonal axis to the primary beam. As the primary and secondary beams are tilted about orthogonal axes, we would expect the binary transmittance function calculated from their interference field to exhibit a structure reminiscent of two crossed gratings: a *pinhole*-like structure. Figure 2(b) shows



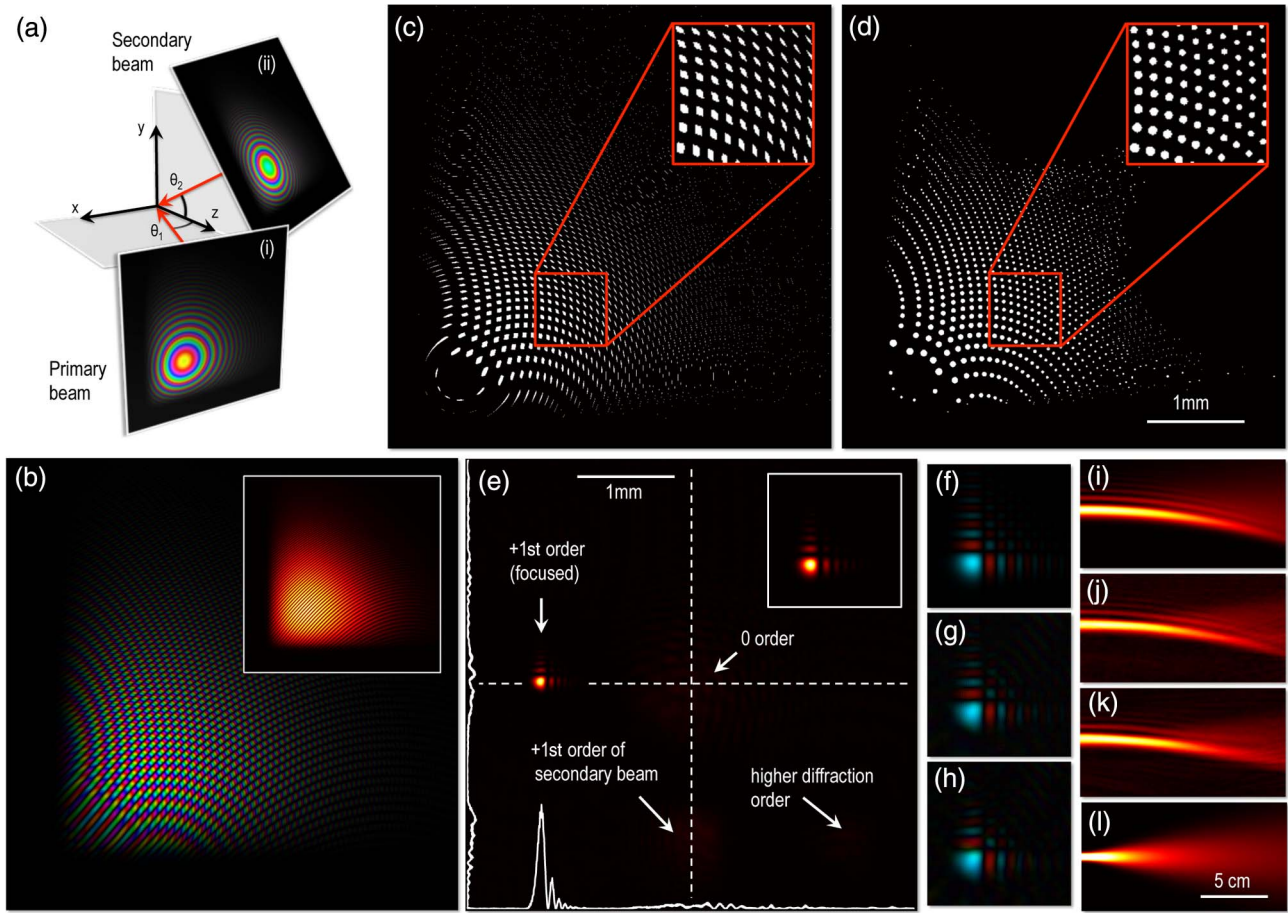


**Fig. 2.** Design of a photon sieve to generate an Airy beam. (a) Schematic showing two beams (*primary* and *secondary*) incident on a plane with orthogonal tilts, at angles  $\theta_1$  and  $\theta_2$ . (b) Field created by the interference of the primary and secondary beams shown in (a),  $\mathcal{D}_{\text{AiryCross}}(x, y)$ . Inset shows the amplitude of the field. (c) Binary transmittance function of a dual beam Fresnel zone plate, calculated from the field in (b) using Eqs. (1)–(3). The choice of the tilt angles of the primary and secondary beams affects both the position and the shape of the apertures in (c). Keeping the tilt angle of the secondary beam the same magnitude as the tilt angle of the primary beam (i.e.,  $\theta_1 = \theta_2$ ) results in apertures that can be well approximated by circular pinholes. (d) Binary transmittance function of an off-axis Airy beam photon sieve,  $T_{\text{AiryPS}}(x, y)$ , formed by replacing each aperture in (c) with a pinhole of equivalent area. Apertures below a threshold area have been removed, and the smallest aperture is  $\sim 5.5 \mu\text{m}$  in diameter. (e) Simulation of the intensity at the focal plane of the photon sieve shown in (d). As required, the Airy beam is the brightest part of the field. Plots at the edge show a cross-section of the relative intensity along the dashed lines. (f)–(h) Comparisons of the simulated phase of the target field (f) with the beam created by the dual-beam Fresnel zone plate (g) and the Airy photon sieve (h). (i)–(l) Comparison of the simulated propagation characteristics of the beams. (i) shows the propagation of the target field shown in (f). (j) shows the propagation of the beam shown in (g) created by the dual-beam Fresnel zone plate. (k) shows the propagation of the beam shown in (h) generated with the Airy photon sieve. (l) shows the propagation of a Gaussian beam of equivalent far-field beam waist to that of the Airy beam, for comparison. The phase scale is the same as used in Fig 1(a).

the amplitude and phase of such an interference field. By keeping the amplitudes of the primary and secondary beams the same, their interference field forms a 2D quasi-periodic array as shown in Fig. 2(b). Therefore, the binary transmittance function of this *dual beam Fresnel zone plate*, calculated as before using Eqs. (1)–(3), is formed from an array of isolated apertures as shown in Fig. 2(c). The diffraction pattern at the focal plane of the dual-beam Fresnel zone plate now contains two first orders, each associated with the primary or secondary beam used to create it. Even though the apertures are not perfectly circular, the dual-beam Fresnel zone plate is very well approximated by replacing each aperture with a circular pinhole of equivalent area, positioned at the center of mass of the original aperture, creating a photon sieve. Figure 2(d) shows an *Airy photon sieve*, of binary transmittance function  $T_{\text{AiryPS}}(x, y)$ , created by following the procedure just described.

Our aim is to create a generalized photon sieve which creates a diffraction pattern in which the target field forms the brightest order. This is important, for example, if the photon sieve were to be used as a lens for imaging, where a single well-defined point-spread function is required. If the amplitude and phase of the primary and secondary beams are identical (except for their orthogonally tilted incident angles), the symmetry of these beams dictates that the focal plane will contain two equally bright copies of the target field. Such a photon sieve and the resulting diffraction pattern are shown in Figs. 3(a) and 3(d), and it can be seen that both have a diagonal line of mirror symmetry. However, there is no requirement for the phase of the secondary beam used to design the sieve to be identical to the first: modifying the secondary beam's phase repositions the apertures, which changes the structure of the diffraction orders of the secondary beam while leaving the primary beam's first diffraction order unaffected.

Therefore, we can take advantage of the phase freedom of the secondary beam to reduce the maximum intensity of light in the secondary diffraction orders. This is the case in Fig. 2, where the cubic phase dependence of the secondary beam has been removed to cancel its quasi-non-diffractive quality and a shorter-focal-length lens term has been applied to refocus it to a different depth. Therefore, the interference field,  $\mathcal{D}_{\text{AiryCross}}$ , used to design the Airy photon sieve from the interference of two crossing beams and shown in Figs. 2(b) and 2(c), is given by

$$\mathcal{D}_{\text{AiryCross}} = C_{\text{Airy}}[e^{i\phi_{\text{pri}}} + e^{i\phi_{\text{sec}}}], \quad (10)$$

$$\phi_{\text{pri}} = \phi_{\text{cub}} + 2\pi u_0 x + \phi_{\text{lens}}(x, y, f_1), \quad (11)$$

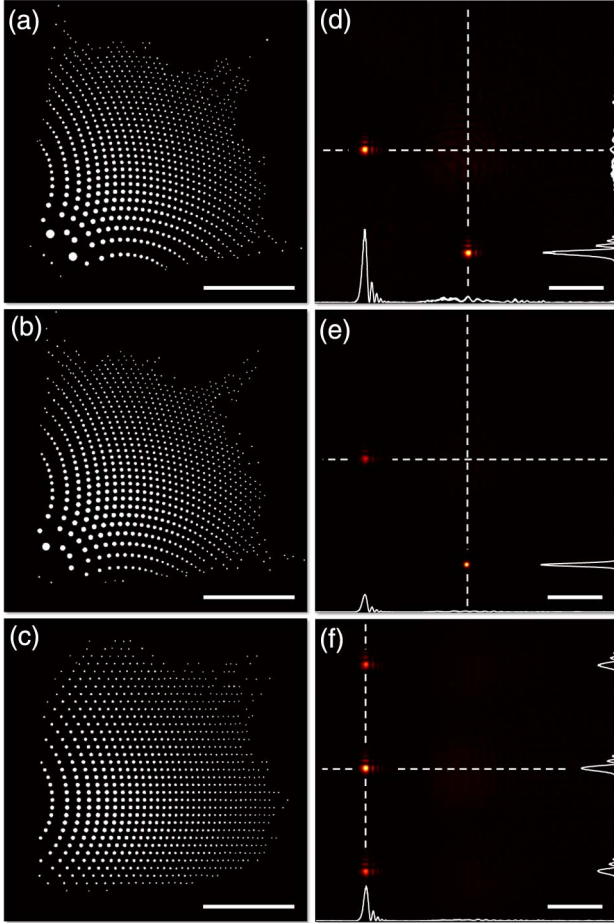


**Fig. 3.** Control of additional diffraction orders. (a)–(c) show three different photon sieve designs (once again, the smallest pinhole diameter in these arrays is  $\sim 5.5 \mu\text{m}$ ), and (d)–(f) show the corresponding simulated diffraction patterns at the focal plane. Relative intensity cross-sections along the dashed lines are plotted at the border of each figure. The primary beam used to design each photon sieve is the same:  $C_{\text{Airy}}e^{i\phi_{\text{pri}}}$ , where  $\phi_{\text{pri}}$  is given by Eq. (11), resulting in the same primary first diffraction order in each case. The phase of the secondary beams varies ( $C_{\text{Airy}}e^{i\phi_{\text{sec}}}$ ), thus changing the nature of the other diffraction orders. In (a),  $\phi_{\text{sec}} = \phi_{\text{pri}}$ , resulting in twin copies of the Airy beam produced in the primary and secondary first orders. In (b), the cubic phase term is dropped:  $\phi_{\text{sec}} = 2\pi u_0 y + \phi_{\text{lens}}(x, y, f_1)$ , so while the secondary order is still focused to the same plane, it no longer exhibits the pseudo-diffraction-free properties of an Airy beam. In (c),  $\phi_{\text{sec}} = 2\pi u_0 y$ , the secondary beam is no longer focused, and the pinholes are positioned in regularly spaced rows, resulting in regularly spaced copies of the Airy beam. Scale bars represent 1 mm.

$$\phi_{\text{sec}} = 2\pi u_0 y + \phi_{\text{lens}}(x, y, f_2), \quad (12)$$

where  $\phi_{\text{pri}}$  and  $\phi_{\text{sec}}$  describe the phase of the primary and secondary beams, respectively. Here,  $f_2 = 0.65f_1$ —a ratio chosen to ensure that the secondary order and any other unwanted “ghost” orders come to a focus outside the specified focal plane of the photon sieve. Figure 2(e) shows the simulated intensity of the Fresnel diffraction pattern at the focal plane of the Airy photon sieve. It can be seen that the maximum intensity of the Airy beam dominates over the maximum intensity of other diffraction orders, as required. Figure 3 shows how the choice of the phase of the secondary beam results in different ghost diffraction orders. In each case, the power radiated into each diffraction order is the same but the peak intensity and form of the additional diffraction orders can be controlled.

Figures 2(f)–2(h) show simulations comparing the target field (f) with the field generated with a dual-beam Fresnel zone plate (g) and the Airy photon sieve (h). It can be seen qualitatively that coercing the apertures into pinholes does not significantly degrade the fidelity of the output beam. Using Eq. (8), we can quantitatively assess the impact of coarse-graining the dual-beam Fresnel zone plate into pinholes. We find a fidelity of  $F = 0.99$  for the beam generated using the dual-beam Fresnel zone plate shown in Fig. 2(c), and  $F = 0.95$  for the beam generated using the Airy photon sieve shown in Fig. 2(d). The high theoretical fidelity of the Airy photon sieve output is further borne out by examining the propagation characteristics of the generated Airy beams. Figures 2(i)–2(k) show simulations comparing the propagation of the Airy beams in Figs. 2(f)–2(h). As the diffraction orders spread in different directions, interference between them is minimal as they propagate and the propagation of the Airy beam generated using the Airy photon sieve (k) is very similar to the propagation of the Airy beam generated by the dual-beam Fresnel zone plate (j) and the target field (i).

### A. Beam Generation Efficiency

As described in Section 3, the generalized photon sieves are designed using a field representing the interference of two crossing beams of equal amplitude. Therefore, we anticipate that their efficiency would be approximately half that of the corresponding generalized Fresnel zone plates described in Section 2. The efficiency of any filter is given by the overlap integral between the required field at the plane of the filter and the actual field at the plane just after the filter itself. Therefore the normalized efficiency of the filters described here,  $E$  ( $0 \leq E \leq 1$ ), is given by

$$E = \left| \frac{1}{N_E} \iint T(x, y) [C(x, y) e^{i(\phi_{\text{filt}} + \phi_{\text{lens}})}]^* dx dy \right|^2, \quad (13)$$

$$N_E = \left[ \iint |T(x, y)|^2 dx dy \times \iint |C(x, y)|^2 dx dy \right]^{\frac{1}{2}}, \quad (14)$$

where  $N_E$  is again the normalization factor and, in this case, the limits of the integrals are set by the edges of the filter. Using Eq. (13), the theoretical efficiency of the Airy Fresnel zone plate shown in Fig. 1(j) is  $E = 15\%$ , compared to  $E = 7\%$  for the Airy photon sieve shown in Fig. 2(d), which agrees well with our prediction.

The efficiency of the generalized photon sieves could potentially be improved by reducing the amplitude of secondary beam compared to the primary beam. We explored this possibility numerically and found that the greater the difference in relative

amplitudes of the primary and secondary beams, the less well-approximated the dual-beam Fresnel zone plate is by pinholes, and so there is a trade-off between generation efficiency and beam fidelity in this approach [38].

#### 4. EXPERIMENTAL DEMONSTRATIONS OF GENERALIZED PHOTON SIEVES

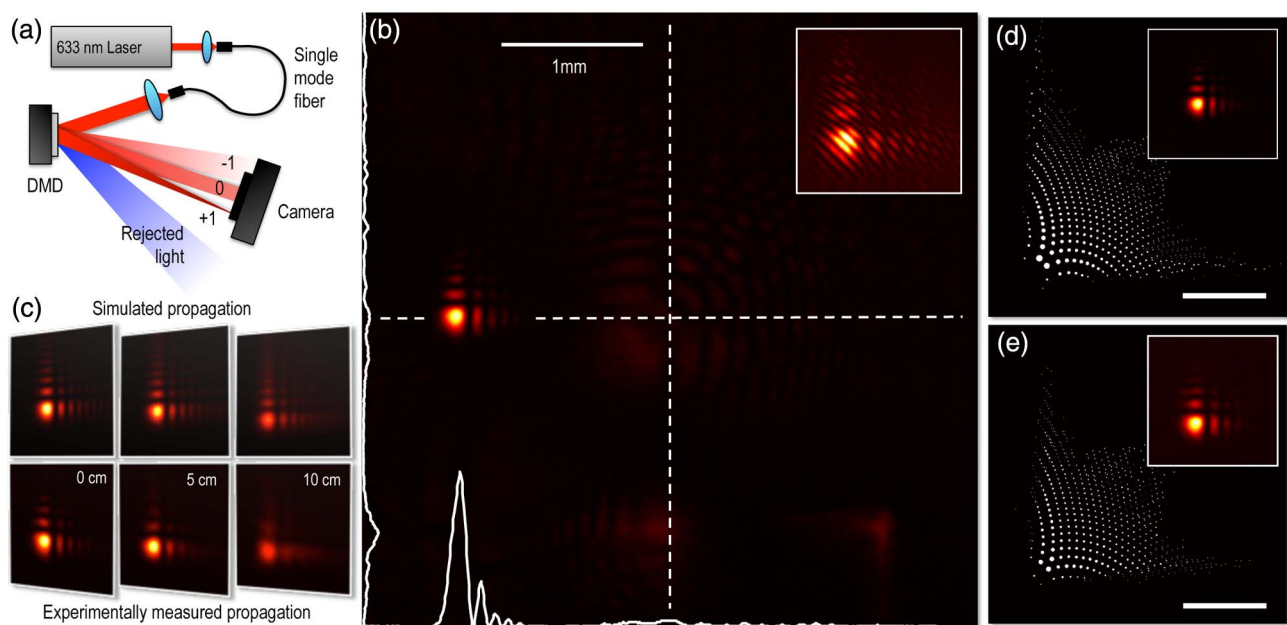
To validate the numerical simulations, we used a DMD to display patterns corresponding to a variety of simple photon sieves and experimentally measured the diffraction pattern at their focal planes. Figure 4(a) shows a schematic of the experimental setup. Figure 4(b) shows the intensity of the Fresnel diffraction pattern at the focal plane of the Airy photon sieve shown in Fig. 4(d), with a focal length of 20 cm. The measured intensity agrees well with that expected from the numerical simulations shown in Fig. 2. To experimentally characterize the phase profile of the resultant beam, we also recorded its interference with a tilted planewave, as shown in Fig. 4(b) inset. As expected, the phase in neighboring intensity lobes of the Airy beam switches by  $\pi$  radians, indicated by the lateral movement of the intensity fringes by half a period in adjacent lobes. The propagation of the Airy beam over a distance of 10 cm is shown in Fig. 4(c) (bottom row) and compares well with a simulation of the propagation of the target field (top row). Figures 4(d) and 4(e) show the pinhole configurations and the corresponding +1st order intensity distributions at the focal plane of the sieve as the focal length is varied: the focal length = 20 cm in

Fig. 4(d) and 25 cm in Fig. 4(e). As expected, the beam in Fig. 4(e) is enlarged due to the lower NA of the photon sieve.

We also used the design principles just detailed to create photon sieves for the generation of a range of additional types of beams. Figure 5 shows the required target fields, photon sieves, and experimentally measured fields for the generation of a Laguerre–Gaussian (LG) mode, a zero-order Bessel beam, Hermite–Gaussian mode, and a petal pattern formed from the superposition of two LG beams. The beams demonstrated in Figs. 5(a), 5(c), and 5(d) are either structurally stable (a, c) or spiral-type (d). These types of beams have intensity profiles which are maintained upon propagation from near to far field except for a magnification and/or rotation (in the case of the spiral type beam). Therefore, it can be seen that the distribution of pinholes in these cases looks like the required amplitude of the target beam itself [40]. As the design method is based on scalar diffraction theory, it is appropriate for the generation of arbitrary scalar fields, limited only in spatial resolution by the minimum pinhole size (providing this is larger than the wavelength of incident radiation) and separation achievable in the manufacture of the sieve or, in our experiment, the resolution of the DMD used to demonstrate the effect.

#### 5. ABERRATION CORRECTION

So far we have considered the design of a photon sieve, assuming it will be illuminated by a plane wave. However, it is also



**Fig. 4.** Experimental verification of an Airy beam photon sieve. (a) Schematic of the experimental setup. An Airy photon sieve,  $T_{\text{AiryPS}}(x, y)$  [shown in (d)] is displayed on a DMD (Texas Instruments DLP3000,  $684 \times 608$  micromirrors, active area of  $3.70 \times 6.57$  mm). We note that the use of a DMD introduces an additional lateral phase tilt due to the offset of the DMD pixels which each pivot about their own axis. We compensate for this by laterally stretching the displayed pattern. The degree of stretch is dependent upon the incident angle of the illuminating beam. This would be unnecessary if fabricating a planar photon sieve. A 633 nm wavelength laser beam was guided through a single-mode fiber to produce a TEM 00 output mode, which is then expanded to overfill the DMD. (b) The intensity of the diffraction pattern from light incident at positions inside the pinholes is observed with a CMOS camera (Hamamatsu ORCA-Flash 4.0) at the focal plane of the photon sieve at distance  $f$  from the DMD. Mirrors corresponding to the positions outside the pinholes transmit light into a rejected order away from the camera. Inset shows the interference of the Airy beam with a plane wave (formed from light scattered from around the active area of the DMD, which was blocked in the main image). (c) Top row: simulated propagation of the required Airy beam showing the intensity at (i) the focal plane, (ii) 5 cm beyond, and (iii) 10 cm beyond the focal plane. Bottom row: experimentally measured intensity of the Airy beam as it propagates the same distances. (d) and (e) Pinhole configurations (the smallest pinhole diameter in these arrays is  $\sim 5.5$   $\mu\text{m}$ ) and corresponding first-order intensity distributions at the focal plane for two different focal lengths of Airy beam photon sieve. Focal length = 20 cm in (d) and 25 cm in (e). As expected, the beam in (e) is enlarged due to the lower NA of the photon sieve. Scale bars in (d) and (e) represent 1 mm.



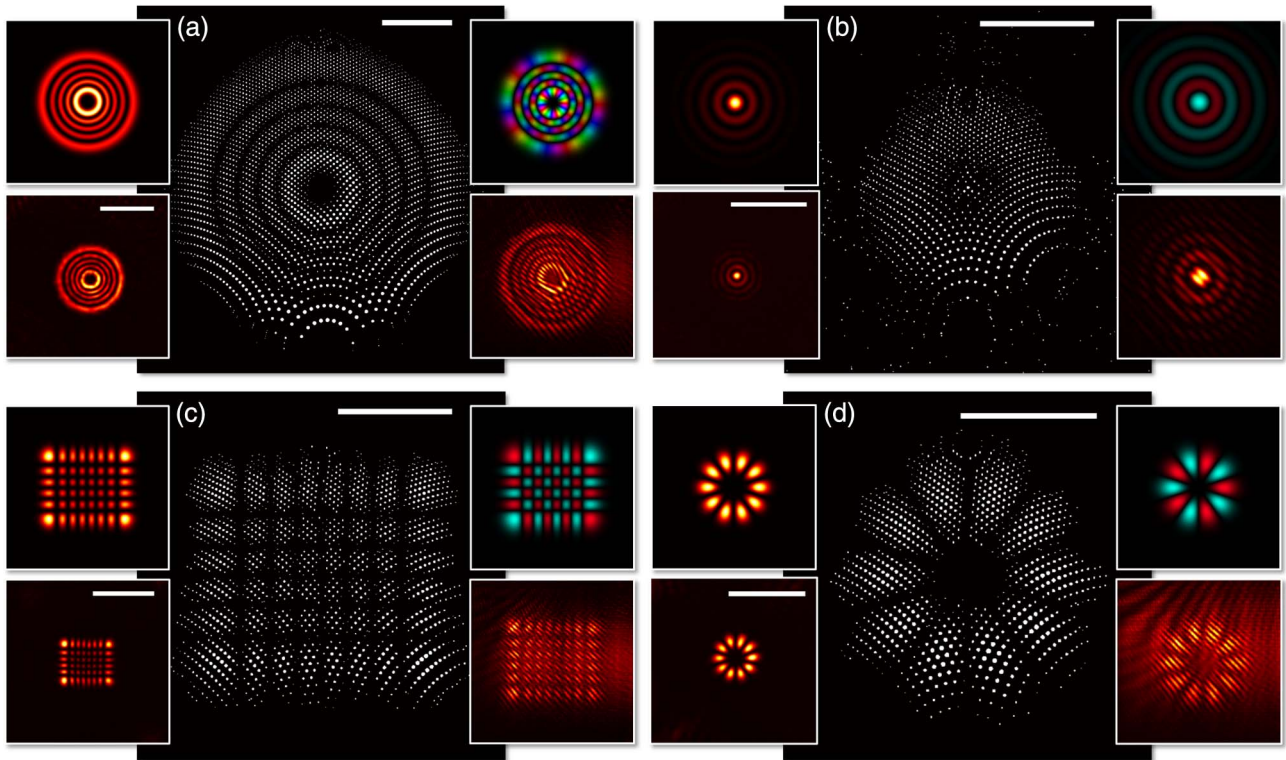


**Fig. 5.** Experimental demonstration of photon sieves to create a range of different spatial modes. The focal length of the photon sieves is 20 cm and the smallest pinhole diameter in these arrays is once again  $\sim 5.5 \mu\text{m}$ . In each case, the insets show the target intensity and phase (top left and right, respectively) and the experimentally measured intensity and plane wave interference pattern (bottom left and right, respectively). In each case, the measured intensity pattern is zoomed out to show the separation of the target beam from other diffraction orders. (a) Laguerre–Gaussian beam carrying a vortex charge of  $\ell = 5$  and radial mode  $p = 4$ . (b) Bessel beam of vortex charge  $\ell = 0$ . To create this, the Fourier transform of a pseudo-diffraction-free Bessel beam was approximated by an annular slit [39]. (c) Hermite–Gaussian beam of mode order  $m = 7$ ,  $n = 5$ . (d) Superposition state of two LG beams of opposite vortex charge  $\ell = \pm 5$ ,  $p = 0$ . Scale bars represent 1 mm. The phase scale is the same as used in Fig 1(a).

straightforward to adapt the design to accommodate an illuminating field other than a plane wave. For example, any phase aberrations  $\phi_{abb}(x, y)$ , found in the incident field or due to any warping of the shape of the sieve itself, can simply be absorbed into the design equation as long as they are known, according to

$$p(x, y) = \phi_C + \phi_{\text{tilt}} + \phi_{\text{lens}} - \phi_{abb}. \quad (15)$$

This adjusts the position of the pinholes so that the beams in the +1st orders of the photon sieve are aberration-corrected. The

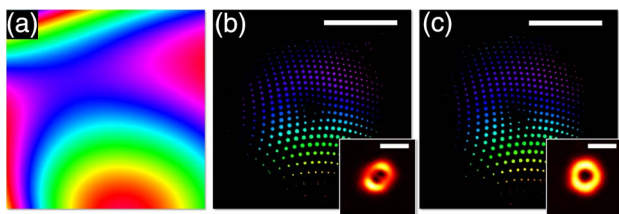


**Fig. 6.** Experimental demonstration of aberration correction of a non-planar illuminating wave. (a) Estimate of the phase front of the beam incident on the photon sieve. (b) Uncorrected photon sieve to generate a LG beam varying a vortex charge of  $\ell = 2$  and radial mode of  $p = 0$ . Inset shows the resultant distorted first-order beam. (c) Aberration-corrected photon sieve, where the positions of the apertures have been adjusted to accommodate the aberrations in the illuminating beam. Inset shows that distortions in the first-order beam are now corrected. Scale bars in (b) and (c) represent 1 mm, and 0.5 mm in the insets. The phase scale is the same as used in Fig. 1(a).

–1st orders, which are complex conjugates of the +1st orders, are consequently doubly distorted. However, the additional distortion of the –1st orders is unimportant, as these orders diverge from the sieve and are diffuse at its focal plane. Aberration correction is experimentally demonstrated in Fig. 6, where the single-mode TEM 00 beam has been deliberately distorted by passing it through a perspex sheet of low optical quality prior to its incidence on the DMD. Figure 6(a) shows an estimate of the phase distortion in the illuminating wave [41]. Figure 6(b) shows an uncorrected photon sieve designed to generate a LG beam carrying a vortex charge of  $\ell = 2$  and radial mode of  $p = 0$ . The apertures are now colored according to the relative phase of the light emanating from them. The inset shows that the first-order beam at the focal plane of (b) is distorted. In Fig. 6(c), the photon sieve has been redesigned according to Eq. (15), incorporating the estimated phase distortion in Fig. 6(a). The inset in (c) shows the first-order LG ( $\ell = 2$ ,  $p = 0$ ) beam, which has now been aberration-corrected.

## 6. DISCUSSION AND CONCLUSIONS

We have described an intuitive method to design generalized photon sieves that can create arbitrarily structured complex fields at their foci. The spatial resolution of the target field is limited by the NA of the sieve. As the NA is increased, smaller and more closely spaced pinholes are required. When the pinhole diameters approach the size of the wavelength of the illuminating radiation,



the assumptions inherent in scalar diffraction theory are no longer valid (which is also true for the features in generalized Fresnel zone plates) [36,42,43]. This places a minimum limit on the size of the pinholes and thus a maximum limit on the NA of the photon sieve and the spatial resolution of the target field. We have shown how to quantify the fidelity and efficiency of our generalized photon sieves using Eqs. (8) and (13). These equations can also be used to assess the impact of pinhole size and shape errors or further coarse-graining (such as limiting pinhole diameters to a discrete range) on the fidelity and output efficiency of the photon sieve.

In our design method, the target beam is formed *off-axis*, enabling creation of a high-fidelity target field from a relatively low number of pinholes by laterally separating it from other diffraction orders at the focal plane. In addition to the design method we have described here, we also note that there is an alternative method to design *on-axis* generalized photon sieves using many more pinholes. For example, the phase distribution shown in Fig. 1(c) could be used as an underlying guide to position pinholes quasi-randomly following the methods described by Kipp *et al.* in [16]. In this alternative approach, the amplitude modulation of the field could be captured with a pinhole density apodization given by  $\sim \text{asinc}(C(x,y)/C_{\text{max}})$ . Following [16], by positioning pinholes of a size which overlaps several Fresnel zones, the numerical aperture of the lens could be increased for a fixed minimum pinhole size. In this case, the peak intensity of the on-axis target field would be much greater than other diffraction orders, therefore rendering interference with the zero diffraction order negligible. However, as there is no in-built control of additional diffraction orders caused by the quasi-random positioning of the pinholes with this strategy, the fidelity of the resultant field may potentially still suffer.

Although photon sieves deliver a slightly lower efficiency than Fresnel zone plates, they offer several other advantages. Photon sieves are simpler to manufacture, as they consist of an array of isolated circular apertures rather than the arbitrarily shaped and high-aspect-ratio apertures that can be present in binary gratings [see Fig. 1(j)]. Photon sieves are also more robust than Fresnel zone plates, as they contain no disconnected material in their design [as in the case of on-axis Fresnel zone plates, which require a supporting structure with which to hold their concentric rings in place, see Fig. 1(d)]. This increased robustness facilitates their fabrication and use, as a high flux of radiation incident on delicate microscale structures can distort and damage them over time [44].

The design principles described in this paper can also be used to design transmissive binary-phase photon sieves, which would significantly increase their efficiency [45]. In this case, the region defined by each pinhole now represents a region that is  $\pi$  phase-shifted relative to the background material. It is also straightforward to adapt our method to design arrays of pinholes that generate the target beam in the far field. In this case, we simply follow the same procedure as outlined above but ignore the propagation step and do not add a lens phase term.

For the creation of structured electron beams, the use of the generalized Fresnel zone plates and photon sieves with controllable focal lengths described in this work potentially introduce more flexibility into where in the optical system the mask can be placed. If used in a scanning electron microscope (SEM), for example, as the positioning of the mask is not constrained to the far field of the sample, it could potentially be placed inside the main

sample chamber, negating any requirement to access the condenser lens of the SEM.

In summary, by considering the interference field created by primary and secondary beams crossing at a small angle, we have demonstrated a direct approach to encoding both amplitude and phase information into an array of pinholes, creating generalized photon sieves. Furthermore, our design method allows incorporation of aberration correction, and enables control over the intensity and form of unwanted additional diffraction orders produced by the photon sieve. In order to validate our simulations, we have experimentally demonstrated our approach at visible wavelengths using a DMD. However, due to the scale invariance of scalar diffraction theory, the generalized photon sieves described in this paper will be most usefully applied to simplify the shaping of radiation in regimes beyond visible light, where SLMs and DMDs cannot be used.

**Funding.** European Research Council (ERC) (192382).

**Acknowledgment.** We are grateful for useful discussions with Johannes Courtial, Neal Radwell, and Sonja Franke-Arnold.

## REFERENCES

1. J. Dumin, J. Miceli, Jr., and J. Eberly, "Diffraction-free beams," *Phys. Rev. Lett.* **58**, 1499–1501 (1987).
2. G. Scott and N. McArdle, "Efficient generation of nearly diffraction-free beams using an axicon," *Opt. Eng.* **31**, 2640–2643 (1992).
3. E. R. Dowski and W. T. Cathey, "Extended depth of field through wavefront coding," *Appl. Opt.* **34**, 1859–1866 (1995).
4. J. Airt and K. Dholakia, "Generation of high-order Bessel beams by use of an axicon," *Opt. Commun.* **177**, 297–301 (2000).
5. G. Siviloglou, J. Broky, A. Dogariu, and D. Christodoulides, "Observation of accelerating Airy beams," *Phys. Rev. Lett.* **99**, 213901 (2007).
6. T. A. Planchon, L. Gao, D. E. Milkie, M. W. Davidson, J. A. Galbraith, C. G. Galbraith, and E. Betzig, "Rapid three-dimensional isotropic imaging of living cells using Bessel beam plane illumination," *Nat. Methods* **8**, 417–423 (2011).
7. F. O. Fahrbach, P. Simon, and A. Rohrbach, "Microscopy with self-reconstructing beams," *Nat. Photonics* **4**, 780–785 (2010).
8. V. Garcés-Chávez, D. McGloin, H. Melville, W. Sibbett, and K. Dholakia, "Simultaneous micromanipulation in multiple planes using a self-reconstructing light beam," *Nature* **419**, 145–147 (2002).
9. K. Dholakia and T. Čížmár, "Shaping the future of manipulation," *Nat. Photonics* **5**, 335–342 (2011).
10. S. Jia, J. C. Vaughan, and X. Zhuang, "Isotropic three-dimensional super-resolution imaging with a self-bending point spread function," *Nat. Photonics* **8**, 302–306 (2014).
11. K. I. Willig, S. O. Rizzoli, V. Westphal, R. Jahn, and S. W. Hell, "STED microscopy reveals that synaptotagmin remains clustered after synaptic vesicle exocytosis," *Nature* **440**, 935–939 (2006).
12. G. Gibson, J. Courtial, M. Padgett, M. Vasnetsov, V. Pas'ko, S. Barnett, and S. Franke-Arnold, "Free-space information transfer using light beams carrying orbital angular momentum," *Opt. Express* **12**, 5448–5456 (2004).
13. N. Simpson, K. Dholakia, L. Allen, and M. Padgett, "Mechanical equivalence of spin and orbital angular momentum of light: an optical spanner," *Opt. Lett.* **22**, 52–54 (1997).
14. M. P. Lavery, F. C. Speirits, S. M. Barnett, and M. J. Padgett, "Detection of a spinning object using light's orbital angular momentum," *Science* **341**, 537–540 (2013).
15. D. Phillips, M. Lee, F. Speirits, S. Barnett, S. Simpson, M. Lavery, M. Padgett, and G. Gibson, "Rotational Doppler velocimetry to probe the angular velocity of spinning microparticles," *Phys. Rev. A* **90**, 011801 (2014).
16. L. Kipp, M. Skibowski, R. Johnson, R. Berndt, R. Adelung, S. Harm, and R. Seemann, "Sharper images by focusing soft X-rays with photon sieves," *Nature* **414**, 184–188 (2001).

17. B. J. McMorran, A. Agrawal, I. M. Anderson, A. A. Herzing, H. J. Lezec, J. J. McClelland, and J. Unguris, "Electron vortex beams with high quanta of orbital angular momentum," *Science* **331**, 192–195 (2011).
18. J. Verbeeck, G. Guzzinati, L. Clark, R. Juchtmans, R. Van Boxem, H. Tian, A. Béch , A. Lubk, and G. Van Tendeloo, "Shaping electron beams for the generation of innovative measurements in the (S)TEM," *C. R. Phys.* **15**, 190–199 (2014).
19. J. Sun, X. Wang, T. Xu, Z. A. Kudyshev, A. N. Cartwright, and N. M. Litchinitser, "Spinning light on the nanoscale," *Nano Lett.* **14**, 2726–2729 (2014).
20. J. Yuan, S. M. Lloyd, and M. Babiker, "Chiral-specific electron-vortex-beam spectroscopy," *Phys. Rev. A* **88**, 031801 (2013).
21. G. D. Love, "Wave-front correction and production of Zernike modes with a liquid-crystal spatial light modulator," *Appl. Opt.* **36**, 1517–1524 (1997).
22. J. A. Davis, D. M. Cottrell, J. Campos, M. J. Yzuel, and I. Moreno, "Encoding amplitude information onto phase-only filters," *Appl. Opt.* **38**, 5004–5013 (1999).
23. B. R. Brown and A. W. Lohmann, "Complex spatial filtering with binary masks," *Appl. Opt.* **5**, 967–969 (1966).
24. W.-H. Lee, "Binary computer-generated holograms," *Appl. Opt.* **18**, 3661–3669 (1979).
25. C. Paterson and R. Smith, "Higher-order Bessel waves produced by axicon-type computer-generated holograms," *Opt. Commun.* **124**, 121–130 (1996).
26. V. Arriz n, U. Ruiz, R. Carrada, and L. A. Gonz lez, "Pixelated phase computer holograms for the accurate encoding of scalar complex fields," *J. Opt. Soc. Am. A* **24**, 3500–3507 (2007).
27. M. Mirhosseini, O. S. Magana-Loaiza, C. Chen, B. Rodenburg, M. Malik, and R. W. Boyd, "Rapid generation of light beams carrying orbital angular momentum," *Opt. Express* **21**, 30196–30203 (2013).
28. J. Verbeeck, H. Tian, and P. Schattschneider, "Production and application of electron vortex beams," *Nature* **467**, 301–304 (2010).
29. N. Voloch-Bloch, Y. Lereah, Y. Lilach, A. Gover, and A. Arie, "Generation of electron Airy beams," *Nature* **494**, 331–335 (2013).
30. V. Grillo, E. Karimi, G. C. Gazzadi, S. Frabboni, M. R. Dennis, and R. W. Boyd, "Generation of nondiffracting electron Bessel beams," *Phys. Rev. X* **4**, 011013 (2014).
31. W. Chao, B. D. Harteneck, J. A. Liddle, E. H. Anderson, and D. T. Attwood, "Soft X-ray microscopy at a spatial resolution better than 15 nm," *Nature* **435**, 1210–1213 (2005).
32. F. Gim nez, J. A. Monsoriu, W. D. Furlan, and A. Pons, "Fractal photon sieve," *Opt. Express* **14**, 11958–11963 (2006).
33. Q. Cao and J. Jahns, "Modified Fresnel zone plates that produce sharp Gaussian focal spots," *J. Opt. Soc. Am. A* **20**, 1576–1581 (2003).
34. A. Vasara, J. Turunen, and A. T. Friberg, "Realization of general non-diffracting beams with computer-generated holograms," *J. Opt. Soc. Am. A* **6**, 1748–1754 (1989).
35. Y. Wang, W. Yun, and C. Jacobsen, "Achromatic Fresnel optics for wide-band extreme-ultraviolet and X-ray imaging," *Nature* **424**, 50–53 (2003).
36. J. W. Goodman, *Introduction to Fourier Optics* (Roberts, 2005).
37. Z. Li, M. Zhang, G. Liang, X. Li, X. Chen, and C. Cheng, "Generation of high-order optical vortices with asymmetrical pinhole plates under plane wave illumination," *Opt. Express* **21**, 15755–15764 (2013).
38. R. Liu, D. Phillips, F. Li, M. Williams, D. Andrews, and M. Padgett, "Discrete emitters as a source of orbital angular momentum," *J. Opt.* **17**, 045608 (2015).
39. R. Vasilyeu, A. Dudley, N. Khilo, and A. Forbes, "Generating superpositions of higher-order Bessel beams," *Opt. Express* **17**, 23389–23395 (2009).
40. J. Courtial, "Self-imaging beams and the Gouy effect," *Opt. Commun.* **151**, 1–4 (1998).
41. A. Jesacher, A. Schwaighofer, S. F rhappter, C. Maurer, S. Bernet, and M. Ritsch-Marte, "Wavefront correction of spatial light modulators using an optical vortex image," *Opt. Express* **15**, 5801–5808 (2007).
42. C. Genet and T. W. Ebbesen, "Light in tiny holes," *Nature* **445**, 39–46 (2007).
43. K. Huang, H. Liu, F. J. Garcia-Vidal, M. Hong, B. Luk'yanchuk, J. Teng, and C. W. Qiu, "Ultrahigh-capacity non-periodic photon sieves operating in visible light," *Nat. Commun.* **6**, 7059 (2015).
44. R. F. Egerton, P. Lee, and M. Malac, "Radiation damage in TEM and SEM," *Micron* **35**, 399–409 (2004).
45. T. R. Harvey, J. S. Pierce, A. K. Agrawal, P. Ercius, M. Linck, and B. J. McMorran, "Efficient diffractive phase optics for electrons," *New J. Phys.* **16**, 093039 (2014).